Perspective Camera Model With Refraction Correction for Optical Velocimetry Measurements in Complex Geometries

Gerardo Paolillo and Tommaso Astarita

Abstract—Camera calibration is among the most challenging aspects of the investigation of fluid flows around complex transparent geometries, due to the optical distortions caused by the refraction of the lines-of-sight at the solid/fluid interfaces. This work presents a camera model which exploits the pinhole-camera approximation and represents the refraction of the lines-of-sight directly via Snell's law. The model is based on the computation of the optical ray distortion in the 3D scene and dewarping of the object points to be projected. The present procedure is shown to offer a faster convergence rate and greater robustness than other similar methods available in the literature. Issues inherent to estimation of the refractive extrinsic and intrinsic parameters are discussed and feasible calibration approaches are proposed. The effects of image noise, volume size of the control point grid and number of cameras on the calibration procedure are analyzed. Finally, an application of the camera model to the 3D optical velocimetry measurements of thermal convection inside a polymethylmethacrylate (PMMA) cylinder immersed in water is presented. A specific calibration procedure is designed for such a challenging experiment where the cylinder interior is not physically accessible and its effectiveness is demonstrated by providing velocity field reconstructions.

Index Terms—Camera calibration, flow visualization, computer vision, perspective camera model, refractive geometry

1 Introduction

Optical measurement techniques, such as Particle Image Velocimetry (PIV), Particle Tracking Velocimetry (PTV) and Laser Induced Fluorescence (LIF), are nowadays extensively applied in both industry and academic research for the experimental investigation of fluid motions of different nature. Such methods generally make use of lasers to illuminate tracer particles seeding the flow and digital cameras to record the scattered light. In a variety of applications, the flow develops around or inside complex geometries (ducted fans, heart valves, packed beds, etc.) and the refraction of the light at the interfaces between the fluid and the solid walls may compromise or even prevent accurate measurements, since it causes image distortions which are only partially captured by the standard camera models. Such issues are relevant also to simple geometric configurations, such as cylinders or spheres, depending on the curvature and thickness of the walls, the viewing directions of the sensors and the ratio of the refractive indexes of the fluid and solid materials. A common solution developed in recent years in the field of experimental fluid mechanics consists in matching the refractive index of the working fluid with that of the solid boundaries of the flow domain [1], [2]. This is typically obtained by using aqueous salt solutions [2], specific organic compounds [3] or mixtures of two or more liquids [4] in combination with common transparent materials, like acrylic, fused quartz and other silicate glasses.

Refractive index matching procedures are essential in configurations comprising multiple fluid/solid interfaces, such as packed beds or rod bundles, since the high number of refractions involved would prohibit correct visualization and measurements. However, their application involves several requirements that are not always easily met, among which are the precise determination of the refractive indexes of the employed materials, the consideration of the physical and chemical properties of the fluid under investigation and the compatibility of reacting substances. Furthermore, in gas applications it is practically impossible to obtain a perfect refractive index matching, due to the significant difference between the refractive indexes of the gases (approximately equal to 1) and those of the most common transparent solids (typical values between 1.3 and 1.6; see [2] for more details), which results in large optical distortions. In such cases, a correct calibration of the optical system is fundamental for accurate 3D reconstructions.

In photogrammetry and computer vision, multi-media geometries have been addressed in several works. A common scenario is represented by imaging through one or more flat refractive surfaces parallel to each other, which is, for instance, inherent to underwater visualization through transparent windows. A review of camera models used in underwater imaging is found in [5], where three categories of methods are identified in the literature: perspective pinhole camera models featuring a different effective focal length and correction terms to compensate for refraction;

• *The authors are with the Department of Industrial Engineering, Università degli Studi di Napoli "Federico II", 80125 Napoli, Italy. E-mail: {gerardo.paolillo, tommaso.astarita}@unina.it.*

Manuscript received 17 Feb. 2020; revised 6 Oct. 2020; accepted 18 Dec. 2020. Date of publication 22 Dec. 2020; date of current version 5 May 2022. (Corresponding author: Gerardo Paolillo.) Recommended for acceptance by C. Theobalt. Digital Object Identifier no. 10.1109/TPAMI.2020.3046467

generic multiple-view-point camera models methods (computing one ray per each pixel); physical models relying on Snell's law of refraction. The reader is referred to the work of Sedlazeck and Koch [5] for further details and relevant references on such methods. This work also provides an error analysis, which shows the inaccuracy of a pure perspective model used for underwater imaging.

Among methods falling in the last of the above-cited categories, it is worth mentioning here techniques based on ray tracing which model directly the refraction from the knowledge of the position, orientation and geometrical and physical properties of the refractive bodies. The method presented in the current work fits in this class, since it integrates the pinhole camera model with a refraction correction computed via ray tracing and Snell's law of refraction. The ray-tracing approach was first adopted by Kotowski [6] and proposed again later by Mulsow [7] for bundle adjustment in multimedia photogrammetry. Later, the work of Belden [8], building on the work of Mulsow [7], numerically investigated the convergence, accuracy and sensitivity of the calibration method as a function of several parameters, such as camera layout, initialization and volume size. In this paper, an experimental verification of the method was also provided for a planar acrylic window separating air from water and mean reprojection errors between 0.1 and 0.2 pixels were reported as a function of the number of cameras employed. More recently, Feng *et al.* [9] used a similar ray-tracing technique to develop a multi-camera calibration method based on the use of a refractive transparent glass calibration board. Beyond analogies with these methods, the model proposed herein adopts a slightly different principle for 3D point projection, i.e., the computation of the optical ray distortion which is implicitly defined by the relative position and orientation of the pinhole focus, the object point and the refractive body. Moreover, the present method inherently handles the occurrence of total internal reflection in the iterative determination of the optical ray distortion.

In the following, the refractive camera model is first introduced in a general framework, suitable for any refractive body configuration. Comparison with previous work is carried out to highlight the strengths of the proposed method, in particular the faster convergence rate of the iterative procedure for the 3D point projection and the greater robustness. Subsequently, issues related to the camera calibration are addressed and feasible strategies are discussed also in the light of numerical simulations. In the final part of the paper, a challenging experiment related to a tomographic PIV investigation of Rayleigh-Bènard convection inside a polymethylmethacrylate (PMMA) cylindrical cell immersed in water is addressed. To the best of the authors' knowledge, this constitutes the first application of a refractive camera model based on ray-tracing and Snell's law to an optical velocimetry experiment in a cylindrical geometry, while previous PTV/PIV investigations have dealt with only planar windows [10], [11].

2 Camera Model

The refractive camera model used in the present work treats the camera as a pinhole and models the image distortions due to the presence of a refractive transparent body via Snell's law. In the following, before presenting the refractive correction, the pinhole camera model is briefly outlined. The employed notation is defined in Fig. 1.

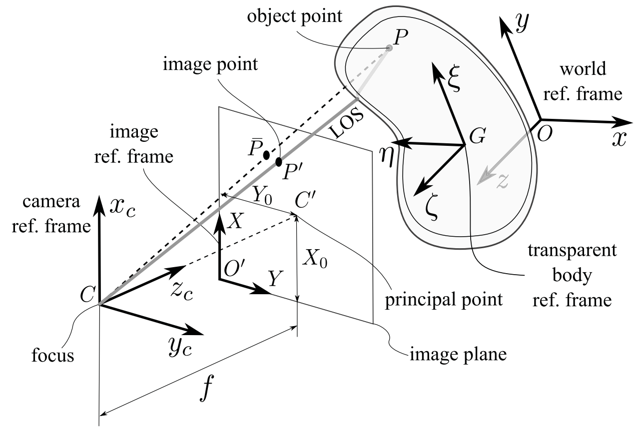

Fig. 1. Perspective projection model with inclusion of a transparent body.

The pinhole camera model [12], [13], [14], [15] is based on perspective projection and includes a distortion model to account for the lens distortions affecting the imaging system. Using homogeneous coordinates, the mathematical relationship between the 2D/3D coordinates is given by

$$c\underline{\mathbf{u}}_{\mathbf{i}} = \mathrm{F}\mathrm{T}_{\mathrm{c}}\underline{\mathbf{x}} \tag{1}$$

$$\underline{\mathbf{X}} = \mathrm{U}(\mathrm{B}\underline{\mathbf{u}}_{\mathbf{i}} + \delta\underline{\mathbf{u}}(\underline{\mathbf{u}}_{\mathbf{i}})). \tag{2}$$

where:

- c is an arbitrary scale factor;
- $\underline{\mathbf{u}}_{\mathbf{i}} = [u_i, v_i, 1]^{\mathrm{T}}$ are the ideal (or undistorted) coordinates of the image point $\bar{P}$ expressed in the camera reference frame $Cx_cy_cz_c$ and in physical units;
- $\underline{\mathbf{x}} = [x, y, z, 1]^{\mathrm{T}}$ are the coordinates of the generic 3D object point P expressed in the world reference frame $Oxyz$;
- the matrices $\mathrm{T_c}$ and F define respectively the coordinate transformation from the world to the camera coordinate system and the scaling transformation; they are expressed as

$$\mathrm{T_c} = \begin{bmatrix} \mathrm{R_c} & \underline{\mathbf{x}}_{\mathbf{c_0}} \\ \underline{\mathbf{0}}^{\mathrm{T}} & 1 \end{bmatrix}, \quad \mathrm{F} = \begin{bmatrix} f & 0 & 0 & 0 \\ 0 & f & 0 & 0 \\ 0 & 0 & 1 & 0 \end{bmatrix},$$

  with $\mathrm{R_c}$ being a 3×3 unitary rotation matrix, generally identified by three Euler angles α_c, β_c, γ_c, $\underline{\mathbf{x}}_{\mathbf{c_0}} = [x_{c_0}, y_{c_0}, z_{c_0}]^{\mathrm{T}}$ the coordinates of the origin O of the world reference frame expressed in the camera coordinate system and f the effective pinhole focal length (distance of the pinhole focus C from the image plane);
- $\underline{\mathbf{X}} = [X, Y, 1]^{\mathrm{T}}$ are the coordinates of the observed image point in the sensor coordinate system $O'XY$;
- $\delta\underline{\mathbf{u}}(\underline{\mathbf{u}}_{\mathbf{i}}) = [\delta u(u_i, v_i), \delta v(u_i, v_i), 0]^{\mathrm{T}}$ is the correction term for the lens distortions;
- the matrices B and U define respectively the correction for the non-orthogonality of the camera sensor

and the transformation from camera to sensor coordinates and they are expressed as

$$\mathrm{B}=\begin{bmatrix}1+b_1 & b_2 & 0\\ b_2 & 1-b_1 & 0\\ 0 & 0 & 1\end{bmatrix},\quad \mathrm{U}=\begin{bmatrix}\chi/d & 0 & X_0\\ 0 & 1/d & Y_0\\ 0 & 0 & 1\end{bmatrix},$$

with b_1 and b_2 being the so-called linear distortion coefficients [13], [14], d the pixel size in the Y-direction, χ the pixel aspect ratio and X_0, Y_0 the image coordinates of the principal point C' (intersection between the principal axis z_c and the image plane) in pixel units.

According to (1), the point P is imaged along a straight line-of-sight (LOS) passing through the focus C and projected into the ideal non-observable image point $\bar{P}$. On the other side, (2) represents the correction of the ideal image coordinates on the account of the imaging distortions and the transformation from the camera coordinate system to the sensor one. Following [16], the image distortions are given by:

$$\delta u(u,v)=u(k_1r^2+k_2r^4)+p_1(r^2+2u^2)+2p_2u\,v+s_1r^2 \tag{3}$$

$$\delta v(u,v)=v(k_1r^2+k_2r^4)+2p_1u\,v+p_2(r^2+2v^2)+s_2r^2, \tag{4}$$

where $r^2=u^2+v^2$ and k_1, k_2 are the coefficients for the radial distortions, p_1, p_2 those for the decentering distortions, s_1, s_2 those for the thin-prism deformation, which are typically neglected (as in the present study).

The parameters α_c, β_c, γ_c, x_{c_0}, y_{c_0}, z_{c_0} identify the camera pose and are called *pinhole extrinsic parameters*. All the remaining parameters (f, b_1, b_2, d, χ, X_0, Y_0, k_1, k_2, p_1, p_2) identify the main features of the imaging process and are called the *pinhole intrinsic parameters*.

With the model defined by (1) and (2), backward ray tracing (from scene to image) is computationally less expensive than forward ray tracing, since, given the 3D object point coordinates $\underline{\mathbf{x}}$, the corresponding 2D image coordinates $\underline{\mathbf{X}}$ can be explicitly computed, while in the opposite case (2) has to be solved iteratively for $\underline{\mathbf{u}}_\mathbf{i}$. For techniques based on forward ray tracing, it is more convenient to use an approximate distortion model based on the application of (3) and (4) to the distorted image coordinates as suggested in [16]. Such a model is defined by the following equations:

$$c(\underline{\mathbf{u}}_\mathbf{d}-\delta\underline{\mathbf{u}}(\underline{\mathbf{u}}_\mathbf{d}))=\mathrm{BFT_c}\underline{\mathbf{x}} \tag{5}$$

$$\underline{\mathbf{X}}=\mathrm{U}\underline{\mathbf{u}}_\mathbf{d}. \tag{6}$$

It is worth mentioning that, although not addressed in the present work, several distortion models providing a closed-form solution for both backward and forward ray tracing have been proposed in the literature [17].

The refraction correction is introduced when one or more transparent bodies (or in general a set of refractive surfaces) are present in the measurement field. For the sake of simplicity, in the following a configuration with only one body as represented in Fig. 1 is considered. The body is arbitrarily shaped, non-deformable, hollow, transparent and homogeneous; its refractive index (n_2) is in general different from both the refractive index of the external fluid (n_1) and that of the internal fluid (n_3) and this causes a refraction of the LOS reaching the generic object point P while crossing the body wall as shown in Fig. 1. The ratios of the refractive indexes of the solid and the surrounding fluids are denoted with the symbols $\varrho_1=n_1/n_2$ and $\varrho_2=n_2/n_3$. More in general, when N refractive surfaces are present in the measurement field, N refractive index ratios have to be defined and these are collected in the vector $\underline{\boldsymbol{\rho}}=[\varrho_1,\varrho_2,\ldots,\varrho_N]^\mathrm{T}$ with $\varrho_i=n_i/n_{i+1}$. For the application of the present model the body geometry is supposed to be defined in a known reference frame $G\xi\eta\zeta$ attached to the body itself. G can be either a specific point of the external or internal surface of the body or another special point such as the centroid or barycenter. Similarly, the ξ, η and ζ-axes can be arbitrary or coincident with one set of the body principal axes. For complex geometries, it is unlikely that the body shape is known in an analytical form; on the contrary, the body surfaces are discretized in a set of planar elements, each of which is assigned a normal unit vector. As concerns simple geometries, an analytical form is indeed available and a small number of parameters can be used to identify the body size and shape: for instance, in the case of a hollow sphere, the geometry is uniquely identified by the internal radius r_i and the wall thickness Δr (supposed to be constant), whereas in the case of a cylinder three parameters are needed, namely the internal radius r_i, the wall thickness Δr and the cylinder height H. More in general, the body size and shape can be parametrized as a function of a finite (although high) number of geometrical quantities, which are collected in the parameter vector $\underline{\mathbf{g}}$. The parameters $\underline{\mathbf{g}}$ and $\underline{\boldsymbol{\rho}}$ are called the *refractive intrinsic parameters*.

The location and orientation of the transparent body reference frame with respect to the world reference frame are identified by six parameters, namely three translations (x_{b_0}, y_{b_0}, z_{b_0}) and three Euler angles (α_b, β_b, γ_b), which allow to transform the coordinates of the generic object point P from the world to the body coordinate system and back via the following relationships:

$$\underline{\boldsymbol{\xi}}=\mathrm{T_b}\underline{\mathbf{x}}=\begin{bmatrix}\mathrm{R_b} & \underline{\mathbf{x}}_{\mathbf{b_0}}\\ \underline{\mathbf{0}}^\mathrm{T} & 1\end{bmatrix}\underline{\mathbf{x}} \tag{7}$$

$$\underline{\mathbf{x}}=\mathrm{T'_b}\underline{\boldsymbol{\xi}}=\begin{bmatrix}\mathrm{R_b^T} & -\mathrm{R_b^T}\underline{\mathbf{x}}_{\mathbf{b_0}}\\ \underline{\mathbf{0}}^\mathrm{T} & 1\end{bmatrix}\underline{\boldsymbol{\xi}}, \tag{8}$$

with $\underline{\boldsymbol{\xi}}=[\xi,\eta,\zeta,1]^\mathrm{T}$, $\mathrm{R_b}$ being the unitary matrix defining rotation from the world to the body reference frame and $\underline{\mathbf{x}}_{\mathbf{b_0}}=[x_{b_0},y_{b_0},z_{b_0}]^\mathrm{T}$ the coordinates of the origin O in the body coordinate system. The parameters α_b, β_b, γ_b, x_{b_0}, y_{b_0}, z_{b_0} are called the *refractive extrinsic parameters*.

When two or more bodies are present, one of them is chosen as a reference and the relative position and orientation of each body with respect to the reference one are defined by as many 6 parameters (3 rotations and 3 translations). Such parameters are added to the refractive intrinsic parameters and stored in the vector $\underline{\mathbf{g}}$ since they identify the geometric layout of the body set, while, in such a case, the

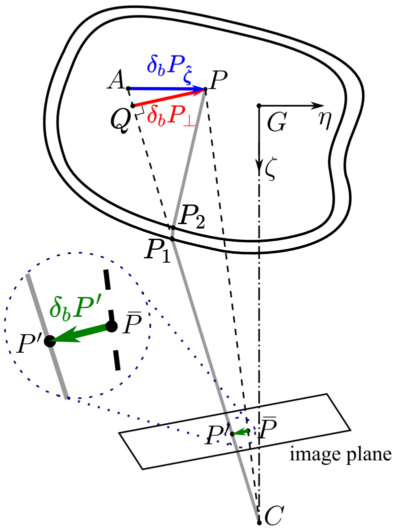

Fig. 2. Definition of the ray and image distortions.

refractive extrinsic parameters identify the location and orientation of the reference body with respect to the world reference frame.

The refractive extrinsic and intrinsic parameters add to the pinhole-camera parameters and allow to model the refraction of the LOSs across the wall of the transparent body. For the purpose of projection of the generic 3D object point, the definition of *optical ray distortion*, which is shown in Fig. 2, is introduced. For simplicity, the LOSs represented in Fig. 2 are supposed to lay in the $\eta\zeta$-plane and the ζ-axis is assumed to be coincident with the line connecting the origin G of the body reference frame with the focus C, while the lens distortions are neglected. The figure shows that the object point P is imaged along the LOS CP_1P_2P and its image is the point P'. In absence of the body, P would be imaged along the LOS CP and its image would be the point $\bar{P}$. The image distortion caused by the refraction of the LOS passing through the body wall is given by $\delta_b P' = P' - \bar{P}$. Conversely, in absence of the body, the actual image P' would result from the LOS CP_1Q, where Q is the normal projection of the object point P on the same undistorted LOS starting from P'. The vector $\delta_b P_\perp = P - Q$ is defined as the *(normal) optical ray distortion* and Q is named as the *(normally) dewarped object point*. The optical ray distortion can be evaluated in infinite different ways as the vector distance from P to the intersection of the undistorted LOS CP_1Q with any plane passing through P. In the following, the refractive camera model is developed using the optical ray distortion evaluated in the plane passing through P and orthogonal to the ζ-axis. This is denoted with the symbol $\delta_b P_{\hat{\zeta}}$ and A is the corresponding dewarped object point.

The idea underlying the present model is shifting the object point P to an arbitrary position on the undistorted LOS $CP'P_1$ and then projecting it according to a standard pinhole camera model. In practice, this is done by computing the optical ray distortion and subtracting it to the real object position, operation hereinafter referred to as *object point dewarping*. The choice of dewarping P to the point A is arbitrary (any other point on the undistorted LOS $CP'P_1$ might be chosen as well) and, as explained below, it is made simply to ease computations.

With the above definitions and adopting an explicit lens distortion model as that in (1) and (2), the perspective camera model with refraction correction can be expressed as follows:

$$\underline{\boldsymbol{\Phi}}(\underline{\boldsymbol{\xi}}_A; \underline{\boldsymbol{\xi}}_C, \underline{\mathbf{g}}, \underline{\boldsymbol{\rho}}) = \mathrm{T_b}\underline{\mathbf{x}} \tag{9}$$

$$c\,\underline{\mathbf{u}}_{\mathbf{i}} = \mathrm{F}\mathrm{T_c}\mathrm{T}'_{\mathrm{b}}\underline{\boldsymbol{\xi}}_A \tag{10}$$

$$\underline{\mathbf{X}} = \mathrm{U}(\mathrm{B}\underline{\mathbf{u}}_{\mathbf{i}} + \delta\underline{\mathbf{u}}(\underline{\mathbf{u}}_{\mathbf{i}})), \tag{11}$$

where $\underline{\boldsymbol{\Phi}}(\underline{\boldsymbol{\xi}}_A) = \underline{\boldsymbol{\xi}}_A + \delta\underline{\boldsymbol{\xi}}(\underline{\boldsymbol{\xi}}_A; \underline{\boldsymbol{\xi}}_C, \underline{\mathbf{g}}, \underline{\boldsymbol{\rho}})$ is the *refractive distortion function*, $\underline{\boldsymbol{\xi}}_A = [\xi_A, \eta_A, \zeta_A, 1]^{\mathrm{T}}$ are the homogeneous coordinates of the dewarped point A, $\delta\underline{\boldsymbol{\xi}} = [\delta\xi, \delta\eta, \delta\zeta, 0]^{\mathrm{T}}$ are the homogeneous components of the optical ray distortion $\delta_b P_{\hat{\zeta}}$ in the body reference frame and $\underline{\boldsymbol{\xi}}_C = [-\mathrm{R_b}\mathrm{R_c^T}\mathbf{x}_{\mathbf{c_0}} + \mathbf{x}_{\mathbf{b_0}}; 1] = [\xi_C, \eta_C, \zeta_C, 1]^{\mathrm{T}}$ are the coordinates of the focus C in the body coordinate system.

In (9) the dependences of the refractive distortion function $\underline{\boldsymbol{\Phi}}$ upon the model parameters have been explicitly reported. In this regard, it should be noted that the optical ray distortion $\delta\underline{\boldsymbol{\xi}}$ depends only on the refractive intrinsic parameters ($\underline{\mathbf{g}}$ and $\underline{\boldsymbol{\rho}}$) and the relative position of the focus C with respect to the body ($\underline{\boldsymbol{\xi}}_C$), and *not* on the relative position and orientation of the body with respect to the world reference frame (refractive extrinsic parameters). Furthermore, $\delta\underline{\boldsymbol{\xi}}$ (or, equivalently, $\underline{\boldsymbol{\Phi}}$) is written as a function of $\underline{\boldsymbol{\xi}}_A$ because the optical ray distortion can be calculated explicitly only when the dewarped location A is given, since the latter along with the focus location C identifies the direction of the undistorted LOS. This is possible by applying Snell's law of refraction as explained in the next section. As concerns the dependence of the refractive distortion function upon the object point body coordinates $\underline{\boldsymbol{\xi}} = \mathrm{T_b}\underline{\mathbf{x}}$, indeed $\delta\underline{\boldsymbol{\xi}}$ only depends on the ζ-coordinate; however, since $\zeta \equiv \zeta_A$, such a dependence can be formally suppressed.

If an approximate implicit lens distortion model is employed as that in (5) and (6), the refractive camera model is expressed by the following equations:

$$\underline{\boldsymbol{\Phi}}(\underline{\boldsymbol{\xi}}_A; \underline{\boldsymbol{\xi}}_C, \underline{\mathbf{g}}, \underline{\boldsymbol{\rho}}) = \mathrm{T_b}\underline{\mathbf{x}} \tag{12}$$

$$c(\underline{\mathbf{u}}_{\mathbf{d}} - \delta\underline{\mathbf{u}}(\underline{\mathbf{u}}_{\mathbf{d}})) = \mathrm{B}\mathrm{F}\mathrm{T_c}\mathrm{T}'_{\mathrm{b}}\underline{\boldsymbol{\xi}}_A \tag{13}$$

$$\underline{\mathbf{X}} = \mathrm{U}\underline{\mathbf{u}}_{\mathbf{d}}. \tag{14}$$

Although this approach avoids iteration for the computation of the lens distortions in forward ray tracing, (12) is still the same as (9) and an iterative procedure is needed to compute the dewarped coordinates $\underline{\boldsymbol{\xi}}_A$ from the assigned world ones $\underline{\mathbf{x}}$. In both the numerical and experimental studies presented below, the model defined by (9), (10), and (11) is used.

3 Computation of the Implicit Optical Ray Distortion

In this section, the computation of the implicit optical ray distortion is discussed in more detail. As aforementioned, such a computation requires iteration. As a first step, a pseudo-code is provided in Algorithm 1 for the computation of the value of the refractive distortion function $\underline{\boldsymbol{\Phi}}$ corresponding to the guess position A^k available at the kth iteration of the solving procedure.

Algorithm 1. Computation of the Refractive Distortion Function: $\underline{\boldsymbol{\xi}}^k = \underline{\boldsymbol{\Phi}}(\underline{\boldsymbol{\xi}}_A^k;\ \underline{\boldsymbol{\xi}}_C, \underline{\mathbf{g}}, \underline{\boldsymbol{\varrho}})$

1: $i = 0$
2: $\underline{\boldsymbol{\xi}}_0^k = \underline{\boldsymbol{\xi}}_C$
3: $\hat{\mathbf{r}}_0^k = (\underline{\boldsymbol{\xi}}_A^k - \underline{\boldsymbol{\xi}}_C)/||\underline{\boldsymbol{\xi}}_A^k - \underline{\boldsymbol{\xi}}_C||$
4: $[\lambda_1^*, \mathcal{S}_1^*] = \text{LOS} \cap \text{Body}\ (\underline{\boldsymbol{\xi}}_0^k, \hat{\mathbf{r}}_0^k, \underline{\mathbf{g}})$
5: $\lambda_A = [(\underline{\boldsymbol{\xi}}_A^k - \underline{\boldsymbol{\xi}}_0^k) \cdot \hat{\boldsymbol{\zeta}}]/(\hat{\mathbf{r}}_0^k \cdot \hat{\boldsymbol{\zeta}})$
6: **while** $\lambda_A > \lambda_{i+1}^* > 0$ **do**
7: $\quad i = i + 1$
8: $\quad \underline{\boldsymbol{\xi}}_i^k = \underline{\boldsymbol{\xi}}_{i-1}^k + \lambda_i^* \hat{\mathbf{r}}_{i-1}^k$
9: $\quad \hat{\mathbf{n}}_i^k : \hat{\mathbf{n}}_i^k \perp \mathcal{S}_i^*$ in $\underline{\boldsymbol{\xi}}_i^k$ and $c := \hat{\mathbf{n}}_i^k \cdot \hat{\mathbf{r}}_{i-1}^k < 0$
10: $\quad$ **if** $d := 1 - \varrho_i(1 - c^2) > 0$ **then**
11: $\quad\quad \hat{\mathbf{r}}_i^k = \varrho_i \hat{\mathbf{r}}_{i-1}^k - (\varrho_i c + \sqrt{d})\hat{\mathbf{n}}_i^k$
12: $\quad$ **else**
13: $\quad\quad$ **return** $\underline{\boldsymbol{\xi}}^k = \underline{\boldsymbol{\xi}}_i^k$
14: $\quad$ **end if**
15: $\quad [\lambda_{i+1}^*, \mathcal{S}_{i+1}^*] = \text{LOS} \cap \text{Body}\ (\underline{\boldsymbol{\xi}}_i^k, \hat{\mathbf{r}}_i^k, \underline{\mathbf{g}})$
16: $\quad \lambda_A = [(\underline{\boldsymbol{\xi}}_A^k - \underline{\boldsymbol{\xi}}_i^k) \cdot \hat{\boldsymbol{\zeta}}]/(\hat{\mathbf{r}}_i^k \cdot \hat{\boldsymbol{\zeta}})$
17: **end while**
18: **return** $\underline{\boldsymbol{\xi}}^k = \underline{\boldsymbol{\xi}}_i^k + \lambda_A \hat{\mathbf{r}}_i^k$
19: **function** $[\lambda^*, \mathcal{S}^*] = \text{LOS} \cap \text{Body}\ (\underline{\boldsymbol{\xi}}, \hat{\mathbf{r}}, \underline{\mathbf{g}})$
20: $\quad \Lambda = \bigcup_{j=1,\dots,N} \{\lambda > 0 : \underline{\boldsymbol{\xi}} + \lambda\hat{\mathbf{r}} \in \mathcal{S}_j\}$
21: $\quad$ **if** $\Lambda = \emptyset$ **then**
22: $\quad\quad \lambda^* = 0$
23: $\quad\quad \mathcal{S}^* = \emptyset$
24: $\quad$ **else**
25: $\quad\quad \lambda^* = \min(\Lambda)$
26: $\quad\quad \mathcal{S}^* = \mathcal{S}_j\ : \underline{\boldsymbol{\xi}} + \lambda^*\hat{\mathbf{r}} \in \mathcal{S}_j$
27: $\quad$ **end if**
28: **end function**

The reader is referred to Fig. 3 for the notation, where an example configuration with only two refractive surfaces is shown. Algorithm 1 is based on the cyclic computation of the intersections P_i^k (identified by the body coordinates $\underline{\boldsymbol{\xi}}_i^k$) of the LOS with the refractive surfaces present along its path and the refractions occurring at each of these interfaces. The initial LOS direction $\hat{\mathbf{r}}_0^k$ is derived from the known dewarped location $\underline{\boldsymbol{\xi}}_A^k$ and the known focus location $\underline{\boldsymbol{\xi}}_C$ (line 3 of the pseudo-code). The first step is computing the intersection between the starting LOS, with parametric equation $\underline{\boldsymbol{\xi}} = \underline{\boldsymbol{\xi}}_0^k + \lambda\hat{\mathbf{r}}_0^k$, and the first refractive surface encountered along its path. The set of operations needed for this purpose is grouped in the subroutine LOS ∩ Body (lines 19-28). For complex configurations, first it is necessary to determine the LOS intersections with each refractive surface $\mathcal{S}_j$ present in the measurement field, which are identified by the parameter values λ ($\lambda > 0$ ensures such intersections to be in the hemisphere of the LOS forward propagation). Λ is the set of all λ related to such intersections; if $\Lambda = \emptyset$ the LOS does not hit any refractive surface, otherwise the first encountered intersection is that characterized by the minimum value of λ in Λ, denoted by λ^*. Computation of the LOS ∩ Body function is the bottleneck of the refractive distortion computation and optimal programming of this function is indeed fundamental for computational speed. Line 5 (Line 16) consists in finding

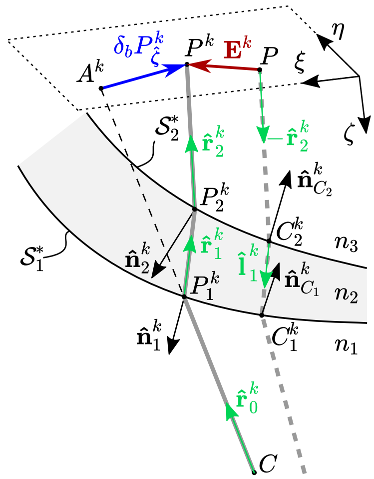

Fig. 3. Detailed schematic of the refraction of the guess LOS CA^k across the body wall for computation of the optical ray distortion of the object point P. Distortions are exaggerated for clarity.

the intersection – identified by the parameter value λ_A – of the starting (current) LOS with the plane passing through A^k and normal to the ζ-axis, in which the ray distortion is calculated (hereinafter, plane of distortion). If this intersection occurs before or at the intersection with the first encountered refractive surfaces ($\lambda_A \le \lambda_{i+1}^*$) or if there occur no further intersections with a refractive surface along the forward-going direction ($\lambda_{i+1}^* \le 0$), then the computed LOS intersection with the plane of distortion is indeed the searched distorted point P^k, the body coordinates of which are given by $\underline{\boldsymbol{\xi}}^k = \underline{\boldsymbol{\xi}}_i^k + \lambda_A \hat{\mathbf{r}}_i^k$. Otherwise, the LOS has not reached the plane of distortion yet ($\lambda_A > \lambda_{i+1}^* > 0$) and has to be propagated across the last hit surface $\mathcal{S}_i^*$. This part of the ray-tracing procedure is drawn in lines 8-14 of the pseudo-code and implies the application of Snell's law, which appears in vector form at line 11. Here, $\hat{\mathbf{n}}_i^k$ is the unit vector normal to $\mathcal{S}_i^*$ and pointing in the direction opposite to the propagating LOS (computed at line 9). The if-condition at line 10 consists in checking the occurrence of a total internal reflection at the surface $\mathcal{S}_i^*$. If $d \le 0$ total internal reflection occurs. In this case, the path followed by the LOS might be very complicated with multiple internal reflections between the refractive surfaces delimiting the optical medium in which the LOS is propagating before exiting with refraction and the final LOS direction might even be opposite to $\hat{\mathbf{r}}_0^k$. In most applications such paths are of limited interest, since they convey information from regions far from the measurement region and due to light absorption along the optical path. Nevertheless, total internal reflection may occur along a guess LOS at the generic kth iteration of the solving procedure, although absent along the actual LOS. This is the reason why in case of total internal reflection the distortion function $\underline{\boldsymbol{\Phi}}$ has been designed to return the point at which the same reflection occurs (line 13). This has a twofold advantage: avoiding the break down of the solving procedure and ensuring a non-zero optical distortion for dewarped points which are not located on the refractive surfaces. If $d > 0$, the LOS crosses the refractive surface and has to be propagated downstream until reaching the plane of distortion (or until a total internal reflection occurs). This is done by repeating cyclically the operations

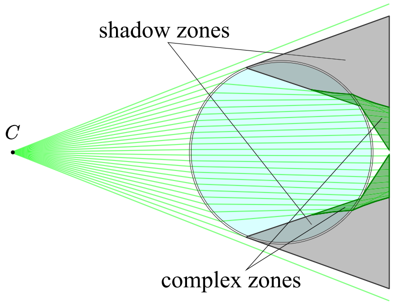

Fig. 4. Occurrence of complex and shadow regions in imaging from air to water through a PMMA cylindrical wall.

in the while-loop at the lines 6-17, starting from the last intersection with a refractive surface $\underline{\boldsymbol{\xi}}_i^k$ and the refracted ray direction $\hat{\mathbf{r}}_i^k$ computed from Snell's law.

The problem of solving (9) for $\underline{\boldsymbol{\xi}}_A$ can be regarded as the problem of finding the zero of the following non-linear equation system:

$$\underline{\mathbf{E}}(\underline{\boldsymbol{\xi}}_A) = \underline{\boldsymbol{\Phi}}(\underline{\boldsymbol{\xi}}_A) - \mathrm{T_b}\underline{\mathbf{x}} = \underline{\boldsymbol{\Phi}}(\underline{\boldsymbol{\xi}}_A) - \underline{\boldsymbol{\xi}} = \underline{\mathbf{0}}. \tag{15}$$

The value $\underline{\mathbf{E}}^k$ of the error function at the kth iteration is also shown in Fig. 3. When projected onto the body axes $\xi\eta\zeta$, (15) is a system of 3 non-linear equations (in homogeneous coordinates the fourth equation is an identity) for only 2 unknowns, namely the dewarped point coordinates ξ_A and η_A, whereas, as aforementioned, from the same definition of the optical ray distortion $\zeta_A = \zeta = (\mathrm{T_b}\underline{\mathbf{x}}) \cdot \hat{\boldsymbol{\zeta}}$. It is worth remarking that the third equation of system (15) (projection along the $\hat{\boldsymbol{\zeta}}$-direction) is not an identity since the third component of $\underline{\boldsymbol{\Phi}}$ is not equal to ζ when a total internal reflection occurs along the LOS path. It is also noted that, working with the normal optical ray distortion introduced in the previous section, (15) would be a square non-linear system with 3 unknowns (the body coordinates of the normally dewarped point Q). Such an approach would be uselessly redundant since the optical ray distortion depends solely on the direction of the undistorted LOS (i.e., $\hat{\mathbf{r}}_0$), which is identified by two parameters.

It is here noted that there exist specific geometric configurations characterized by the presence of shadow or complex zones where (15) has no or multiple solutions, respectively. In order to clarify this issue, Fig. 4 reports the case of a PMMA cylinder surrounded by air from the external side and water from the internal side. The figure has been obtained numerically by choosing the following values of the refractive indexes: $n_1 = 1$, $n_2 = 1.49$ and $n_3 = 1.33$. In such a configuration, it is possible to detect the presence of complex zones (dark green) where the same points are seen along different LOSs and shadow zones (gray) which are reached by no LOS both inside and in the rear part of the cylindrical body. It is clear that when applying any iterative method in complex regions, the procedure converges to only one of the zeros of the error function, whereas convergence is never reached in shadow zones, where the method returns at least a local minimum of the error function. If not managed appropriately, both these behaviors can result in errors for techniques based on backward ray tracing or projection of 3D points.

Since (15) is a system of 3 equations in 2 unknowns with potentially no or multiple zeros, it is clear that a solution of the same has to be found in a non-linear least squares sense. However, in configurations where there are no complex or shadow zones and total internal refraction occurs only in small regions near the body sidewall, (15) reduces to a system of 2 equations in 2 unknowns and a Newton-Raphson method converges to a zero of the error function in very few iterations (typically less than 5). For robustness in the most general case, it is suggested to use a Levenberg-Marquardt method [18] starting with a very small initial value of the dampening factor, in such a way to ensure a convergence rate as near as possible to that of the Newton-Raphson method. Since, generally refractive distortions are expected to be not so severe, the iterative method is initialized with $\underline{\boldsymbol{\xi}}_A^0 = \underline{\boldsymbol{\xi}}$, i.e., assigning the dewarped point location coincident with the object point one.

3.1 Comparison With Previous Work

The camera model proposed in the current paper represents refraction using ray tracing. As above-mentioned, previous models relying on such an approach are found in the works of [6], [7], [8]. The methodology used in [7] and [8] is based on a principle different from that proposed in the current work, namely the determination and projection of the so-called *piercing point*. The piercing point is the intersection point of the LOS with the first encountered interface (that nearest to the camera) and has been denoted with P_1 in Figs. 2 and 3. Also the iterative procedure for computation of the piercing point is basically different from the present method and relies on the alternating forward-ray tracing (AFRT) algorithm. For a detailed description of the latter, the reader is referred to the work of [8]; in the following, the underlying principle is merely described for the purpose of comparison with the present methodology.

Each iteration of the AFRT procedure consists essentially of two steps: first the guess LOS is propagated from the focus C to the optical medium where the object point P is located thus determining the locations of the surface intersection points P_i along the forward-ray path; then the LOS is propagated back from P to C thus determining the locations of the surface intersection points C_i along the backward-ray path. The forward-ray and the backward-ray paths are both represented in Fig. 3. Convergence is reached when the maximum distance $e = \max_i ||P_i^k - C_i^k||$ between the corresponding intersections computed along the forward-ray and the backward-ray paths is lower than a fixed threshold. The procedure is initialized choosing $\hat{\mathrm{r}}_0^k$ as coincident with the direction of the line connecting the focus with the object point. At each iteration the backward-ray path is computed starting with a direction equal and opposite to the direction of the last refracted ray along the forward-path (in the example of Fig. 3 the backward path is computed starting from P with the direction $-\hat{\mathrm{r}}_2$). After determining all the intersections on the backward-ray path, if convergence is not reached, at the next iteration a refined position P_1^{k+1} of the piercing point is obtained by projecting the middle point $(P_1^k + C_1^k)/2$ onto the surface $\mathcal{S}_1^*$; then the new guess $\hat{\mathrm{r}}_0^k$ is identified as the direction of the line connecting P_1^{k+1} and C.

As also recognized by Belden [8], the AFRT procedure suffers from the relevant issues of slow convergence rate and break down in case of total internal reflection either

TABLE 1
Comparison of Convergence Rates of Iterative Methods for (15) and AFRT Procedure [8] in Terms of the Average Number of Computations of the Optical Paths Per Point

method	$\underline{\xi}_0^k = \underline{\xi}$	$\underline{\xi}_0^k = \underline{\xi} - \delta\underline{\xi}(\underline{\xi})$
Gauss-Newton for (15)	4.8	5.1
Levenberg–Marquardt for (15)	21.3	12.1
AFRT procedure [8]	107.3	107.3

along the forward-ray path or along the backward-ray path. The slow convergence rate is essentially related to the underlying guess update method, which does not exploit the error evaluation at each iteration for the estimation of the new guess piercing point and implies the redundant computation of both the forward-ray and the backward-ray paths. Indeed, even from a purely theoretical viewpoint, there is no need to compute the backward-ray path since Snell's law of refraction respects the Helmholtz reciprocity principle and the only sufficient condition to be satisfied is that the propagating LOS reaches the object point P.

Table 1 reports a comparison between the convergence rates of the iterative methods for (15) and the AFRT procedure. The different iterative methods have been tested in the case of a cylindrical body with properties similar to those of the cylinder employed in the experimental tests reported in Section 6 but immersed in air ($r_i = 37$ mm, $\Delta r = 3$ mm, $\varrho_2 = 1/\varrho_1 = 1.49$). Also the distance of the focus from the cylinder axis is similar to that of the experiments (approximately $12.5\, r_i$). The comparison is based on the average number of computations of the optical paths (both forward and backward) per point, computed on 10^3 sample points distributed randomly inside the cylinder interior over a volume extending along the cylinder axis for about $2r_i$ (one internal diameter). For each case, the computations have been repeated 100 times and the results have been averaged. Table 1 shows the faster convergence rate of the present method in comparison to the AFRT procedure; in particular, the Gauss-Newton method shows a faster convergence rate than the Levenberg-Marquardt one. It is also noted that an improvement for the convergence rate of the Levenberg-Marquardt method is obtained by using as initial guess the object point location $\underline{\xi}$ corrected by its optical ray distortion $\underline{\xi}_0^k = \underline{\xi} - \delta\underline{\xi}(\underline{\xi})$ (third column), whereas the AFRT procedure and the Gauss-Newton method seem quite insensitive to initialization.

As concerns the issue of total internal reflection, previous works have not proposed any concrete solution; rather, in the numerical simulations of [8], the control points used in the virtual calibration with cylindrical refractive surfaces were placed not too close to the wall to avoid occurrence of total internal reflection. However, on the experimental side, this is not the best practice since the control points in the regions adjacent to the wall are those affected by the greatest optical ray distortions and thus they contribute more to lead the non-linear procedure for parameter estimation towards a reliable solution, as commented below.

4 Calibration Procedure

Since the proposed refractive camera model relies on the physical laws of perspective and refraction, all these parameters have a clear meaning and their values can be readily estimated and checked after calibration. Due to the non-linear nature of the lens and refraction corrections, the model calibration might be burdensome and involve non-linear least squares optimization in the most general case.

It is here remarked that the problem of calibrating flat refractive geometries, which is very common in underwater imaging, has been dealt with in numerous works [19], [20], [21]. Among these, the work of Agrawal *et al.* [21] developed a general theory for a multi-layer flat refractive geometry. The only requirement of their method is that the camera has to be previously internally calibrated. For configurations involving curved geometries, such as a cylindrical body, it is not so straightforward to obtain a general theory since the flat refraction constraint (i.e., condition that each refracted ray is parallel to the starting ray) does not hold and calibration has to be performed necessarily via non-linear optimization.

When possible, it is convenient to calibrate the pinhole and the refractive parameters separately. In principle, the most desirable scenario would involve sequentially the following steps:

- offline calibration of the intrinsic camera parameters;
- estimation of the camera pose in absence of the refractive body;
- calibration of the refractive parameters with the body placed in situ;
- non-linear refinement of all the parameters.

While generally the intrinsic camera parameters can be calibrated offline, prior camera pose estimation in absence of the body might be difficult and even impossible when the refractive body cannot be moved from its location. In such cases, the pinhole extrinsic parameters and the refractive parameters have to be estimated simultaneously via non-linear least squares optimization. As concerns the third step of the above procedure (calibration of the refractive body parameters), when the body is not accessible from the inside, calibration can be performed by putting the target behind it. This approach may even be preferable than introducing the target inside the body, since points which are imaged along LOSs crossing both sides of the body are generally affected by greater distortions and this may ensure a lower sensitivity of the calibration algorithm to the noise in the image. Such a strategy is adopted in the experiments presented in the following.

5 Numerical Simulations

In this section, insight into the effects of image noise and volume size of the calibration point grid on the estimation of the refractive parameters is provided. Fig. 5 reports the results of a set of numerical simulations of calibration performed with a PMMA cylindrical body (refractive index equal to 1.49) surrounded by water (refractive index equal to 1.33) both from inside and from outside. The numerical tests were performed in conditions similar to those of the experiments presented in the next section, namely $r_i = 37$ mm, $\Delta r = 3$ mm and $\varrho_1 = 1/\varrho_2 = 0.89$; the cameras image the entire width of the cylinder under an angle of view of 7° and their intrinsic parameters are supposed to be known

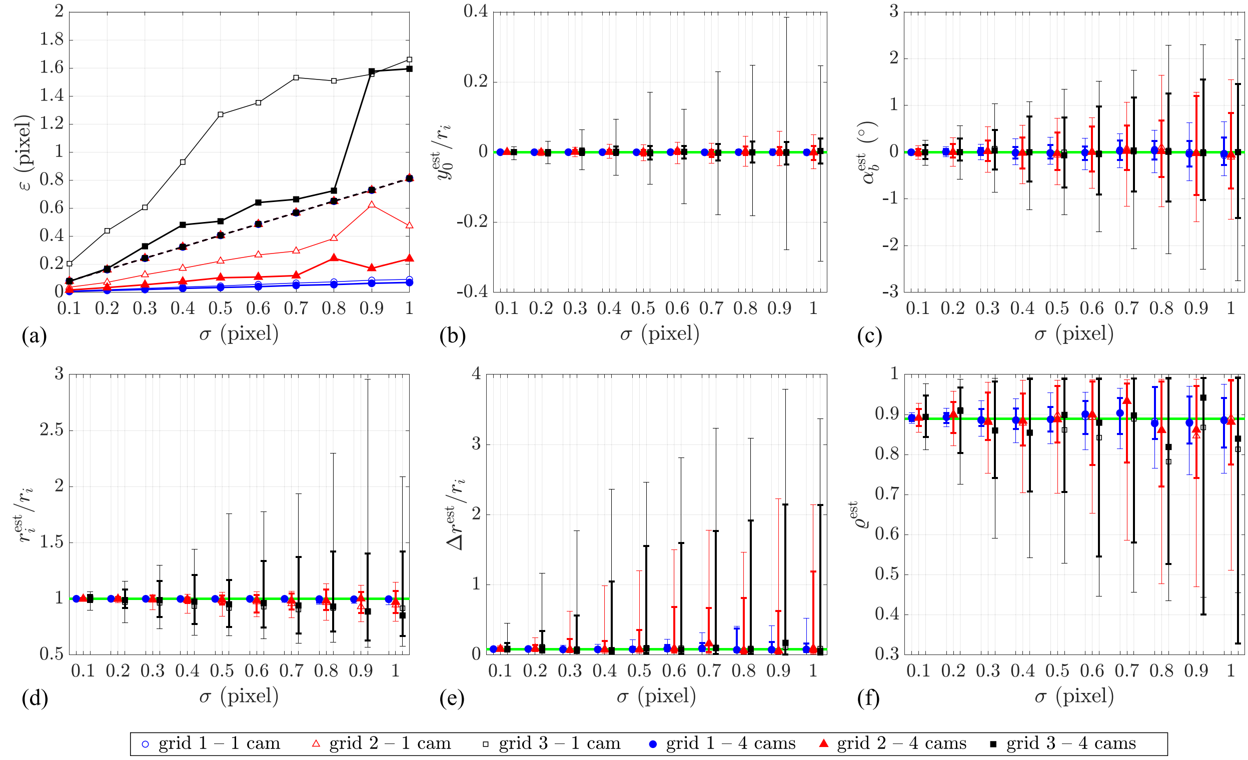

Fig. 5. Calibration results from numerical simulations of a PMMA cylinder surrounded by water for different control point grids and camera bundles (single camera versus 4-cameras bundle): (a) behavior of true modeling error $\varepsilon_{\text{true}}$ (solid lines) and calibration reprojection error $\varepsilon_{\text{calib}}$ (dashed lines) as a function of the Gaussian noise; (b-f) estimated values of the cylinder parameters, respectively: origin shift y_{0_b}, axis angle α_b, internal radius r_i, wall thickness Δr and refractive index ratio ϱ. The green lines represent the exact parameter values.

(the camera point of view is supposed to be placed in water, for simplicity).

The cylinder orientation is clearly identified by only two angles α_b and β_b which determine the direction of its axis with respect to the world reference frame; moreover, by treating the cylinder as infinite, only the two coordinates y_{b_0} and z_{b_0} are necessary to identify the body frame origin (the translation along the cylinder axis can be arbitrarily assigned). For simplicity, the cylinder extrinsic parameters are all assigned to zero ($\alpha_b = \beta_b = 0°$ and $y_{b_0} = z_{b_0} = 0$ mm). Numerical calibration is performed with three different grids (or better clouds) of 512 randomly-distributed control points. The grids differ in the maximum radial distances from the cylinder axis at which the control points are placed, which are $0.9\,r_i$, $0.7\,r_i$ and $0.5\,r_i$, respectively for grids 1, 2 and 3. Gaussian noise is assigned to the image coordinates of the 3D point projections and varied from 0.1 to 1 pixels. Results are presented for both a single camera and a bundle of four cameras arranged in a plane orthogonal to the cylinder axis at the same distance from the latter and angularly spaced of $40°$. The Levenberg-Marquardt algorithm was used for non-linear optimization starting from the exact solution.

The diagram in Fig. 5a reports the behavior of the true modeling errors $\varepsilon_{\text{true}}$ (solid lines) and the calibration reprojection errors $\varepsilon_{\text{calib}}$ (dashed lines) as a function of the Gaussian noise. $\varepsilon_{\text{true}}$ is computed as the root mean square of the image distances between the control point projections and their reference image positions, devoid of the Gaussian noise. Such values have been obtained by averaging the results of all the performed simulations (60 repetitions for the 4-cameras bundle and 240 for the single cameras). It is fundamental to remark that while $\varepsilon_{\text{calib}}$ is computed on the employed calibration grid for each case, $\varepsilon_{\text{true}}$ is always computed on grid 1, thus it conveys information about the error made by extrapolating the model outside the calibration grid (for the cases corresponding to grids 2 and 3). The curves of the reprojection errors are all coincident and have in fact a linear trend. As expected, the true modeling error diverges faster as the Gaussian noise increases when the volume size of the calibration grid is reduced, due to the increasing error made in extrapolating the model. The bundle arrangement (curves with filled markers) however ensures lower errors on the average than the single camera arrangement (unfilled markers) for each of the investigated cases.

Figs. 5b, 5c, 5d, 5e, and 5f show the behavior of the estimated cylinder parameters appropriately normalized. The parameters z_{b_0} and β_b are omitted for conciseness, but their behavior is similar to that of y_{b_0} and α_b. In these diagrams, values corresponding to the three different grids were slightly shifted along the abscissa axis for clearness of presentation. The markers represent the median values of the parameter estimates over the whole set of numerical simulations performed, while the vertical bars extend from the 5th percentile to the 95th one and they are representative of the uncertainty in the parameter estimation. For the calibration grid 1, the errors made on the estimation of the cylinder parameters are considerably small independently of the image noise. As the image noise increases, an increasing uncertainty is observed for the sidewall thickness and the refractive index ratio, with better results for the cameras

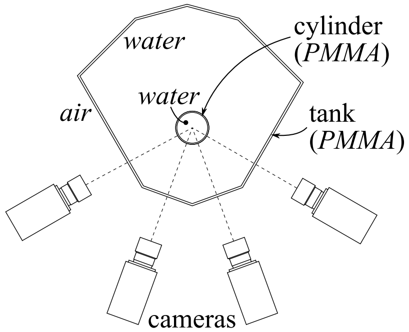

Fig. 6. Schematic of the experimental apparatus showing the configuration of cameras and refractive bodies.

bundle. The same trend is basically observed also for grid 2, although with greater variability of the estimated parameters. As concerns the results of grid 3, when increasing the image noise, large errors in the parameter estimation are found also for the internal radius r_i in addition to Δr and ϱ. On the other side, the cylinder position and orientation are estimated with good accuracy even with considerably high image noise at least for the camera bundle, since the origin position error is typically a small percentage of the radius, whereas the angle error is less than 2°. Both such errors have been observed to produce a contribution to the true modeling errors of at most 0.1 pixels for the present configuration, which is comparable to the lower value of image noise assigned in the present numerical tests.

The above analysis teaches two fundamental lessons: on one side, in a refractive body calibration control points affected by considerable ray distortions (in the case of a cylinder, those close to the sidewall) must be employed in order to achieve a high accuracy in both projection of 3D points and estimation of the body parameters; on the other side, when control points cannot be placed sufficiently close to the curved walls, a more robust approach is measuring physically the refractive intrinsic parameters and using image analysis only to estimate the extrinsic parameters. This procedure should be also preferred when data is particularly noisy, since the extrinsic parameters have been observed to be less affected by image noise and recovered with greater accuracy. Such considerations have been taken into account in the design of the calibration procedure for the experiment presented below.

6 Experimental Application

6.1 Calibration of the Refractive Model

In this section the calibration results from real experiments are presented. These are related to a tomographic PIV investigation of thermal convection inside a PMMA cylinder immersed in a water tank. The experimental setup is schematically shown in Fig. 6. Four sCMOS Andor Zyla cameras with a resolution of 2560×2160 pixels and 28-mm focal length lenses (Nikon AF Nikkor 28mm f/2.8D wide-angle lenses) are used. The cameras are arranged in a planar configuration and mounted on Manfrotto 3-Way tripod heads which are stably secured to apposite frames (made up of aluminum rails). All the equipment is positioned on an optical table and left intact during the present experiments. The cameras image the cylinder through PMMA windows with a thickness of 5 mm. The camera axes are roughly set orthogonal to the tank windows, resulting in a relative angular spacing of approximately 40°. The nominal distance of the internal side of each window from the cylinder axis location is 171 mm. The cylinder internal radius is 37 mm and its sidewall thickness is 3 mm. More details about the experimental setup are found in [22].

Optical calibration is performed in three steps:

1) target-based pinhole/window calibration in absence of the cylinder: a calibration plate consisting of a regular grid of black dots on a white background (dot diameter equal to 0.5 mm and spacing of 5 mm in both directions) is recorded at six known positions, reached by translating the same target along the z-direction (normal to its plane) with a regular spacing equal to 10 mm. The target is not rotated during translation;
2) target-based cylinder calibration: the calibration plate is kept in the final position of its excursion and the cylinder is placed in situ in front of it. One image of the target distorted by the cylinder (and spanning its entire width) is taken by each camera;
3) particle-based self-calibration: water inside the cylinder is seeded with fluorescent polyethylene microspheres which are illuminated by a cylindrical light beam from the top of the cylinder obtained by a Nd: YAG laser; particle images are recorded and the model parameters are further refined via the triangulation procedure of [23] and [24].

It is worth noting that, although the investigated configuration comprises simple geometries (planar windows and a cylinder), camera are calibrated in a fairly complex scenario. In particular, in step 2 the estimation of the cylinder refractive parameters is performed by using control points imaged across three pairs of refractive surfaces, namely both sides of the planar window, both sides of the front part of the cylinder (which are convex surfaces) and both sides of the rear part of the cylinder (concave surfaces). Moreover, although the camera viewing angles are at most around 6°, the angles of incidence of the LOSs on the cylinder surfaces (which determine the magnitude of the corresponding refraction) range from 0° to more than 60°. This ultimately results in large observed image distortions up to 40 pixels (10 pixels on the average).

Cameras are not internally calibrated before step 1. In this first step, both pinhole parameters and PMMA window parameters are determined via image analysis. First, a procedure similar to [14] is used to estimate the pinhole-camera parameters for each camera separately by neglecting the presence of the PMMA window and using the 3D/2D coordinate pairs found in step 1. The corresponding results are reported in the first column of Table 2. Here, among intrinsic pinhole parameters, only the value of f is shown; in the present experiment, the lens distortions are small compared to the refractive ones (approximately 10 percent of the latter), thus the corresponding model parameters are omitted for conciseness. At this stage, although estimates of the camera axis location and orientation near to the actual values are retrieved, the refraction of the LOSs across the window results in a focal length and focus distance from the wall for the water-calibrated perspective model greater than the

TABLE 2
Calibration Reprojection Errors and Estimates of Some Parameters of the Refractive Camera Model With the Tank Windows and the Investigated Cylinder Through the Different Steps of the Experimental Calibration Procedure

	pinhole calib.[1]	pinhole+wind. calib.[1]	pinhole+wind.+cyl. calib.[2]	self-calib.[3]
cam#0, $\varepsilon_{\text{calib}}$ (pixel)	0.302	0.307	0.672	0.155
α, β, γ (°)	$-160.53, 0.26, -0.10$	$-160.14, 0.26, 0.25$	$-161.05, 0.27, -1.34$	$-160.65, 0.26, -1.27$
$x_{c_0}, y_{c_0}, z_{c_0}, f$ (mm)	$-1.52, -5.88, 408.57, 39.24$	$2.09, -10.02, 348.98, 29.40$	$-13.98, -0.33, 349.50, 29.40$	$-13.48, -4.79, 349.66, 29.54$
α_w, β_w (°), z_{w_0} (mm)	-	$-158.80, 1.27, -171.001$	$-162.95, -4.83, -171.001$	$-160.92, -4.78, -169.554$
cam#1, $\varepsilon_{\text{calib}}$ (pixel)	0.329	0.329	0.355	0.194
α, β, γ (°)	$160.36, -0.03, 0.47$	$160.73, -0.03, 0.77$	$160.82, -0.03, -0.46$	$160.52, -0.03, 0.08$
$x_{c_0}, y_{c_0}, z_{c_0}, f$ (mm)	$2.73, -17.36, 419.60, 41.09$	$5.99, -21.24, 357.33, 30.80$	$-7.17, -22.10, 357.28, 30.80$	$-1.84, -18.89, 360.52, 30.85$
α_w, β_w (°), z_{w_0} (mm)	-	$161.80, 1.67, -171.001$	$162.13, -3.33, -171.001$	$160.88, -1.61, -182.405$
cam#2, $\varepsilon_{\text{calib}}$ (pixel)	0.292	0.289	0.526	0.173
α, β, γ (°)	$-120.70, 0.63, -1.20$	$-121.04, 0.63, -0.72$	$-121.15, 0.64, -1.86$	$-121.28, 0.64, -1.58$
$x_{c_0}, y_{c_0}, z_{c_0}, f$ (mm)	$-11.44, 8.19, 402.85, 38.80$	$-6.75, 11.65, 345.29, 29.11$	$-18.27, 12.68, 344.33, 29.06$	$-15.94, 13.69, 345.32, 29.09$
α_w, β_w (°), z_{w_0} (mm)	-	$-122.04, 0.64, -171.000$	$-122.54, -3.96, -171.000$	$-122.72, -3.29, -173.157$
cam#3, $\varepsilon_{\text{calib}}$ (pixel)	0.397	0.398	0.435	0.200
α, β, γ (°)	$118.45, -0.02, 0.23$	$118.56, -0.03, 0.26$	$117.00, -0.05, 0.05$	$117.00, -0.05, 0.01$
$x_{c_0}, y_{c_0}, z_{c_0}, f$ (mm)	$-0.39, 15.09, 427.82, 41.17$	$0.16, 13.99, 363.49, 30.86$	$-3.72, 30.28, 361.08, 30.70$	$-3.82, 30.60, 362.33, 30.72$
α_w, β_w (°), z_{w_0} (mm)	-	$118.78, 0.495, -171.000$	$112.974, -1.710, -171.000$	$112.67, -1.61, -174.740$
cylinder param.				
α_b, β_b (°)	-	-	$-0.535, 0.666$	$-0.535, 0.566$
y_{c_0}, z_{c_0} (mm)	-	-	$-4.29, -4.03$	$-4.25, -4.15$
$r_i, \Delta r$ (mm), ϱ	-	-	$37.00, 3.00, 0.89000$ (fixed)	$37.07, 3.02, 0.88919$

[1]*related to target-based pinhole/window calibration in absence of the cylinder (see text for explanation)*
[2]*related to target-based cylinder calibration (see text for explanation)*
[3]*related to particle-based self-calibration (see text for explanation)*

actual ones. The refractive model with the PMMA window is calibrated via non-linear optimization starting from the pinhole parameters in the first column of Table 2 and the corresponding results are reported in the second column of the same table. It should be noted that the orientation and location of the window are identified by only three parameters, namely two angles (α_w, β_w) and one translation (z_{w_0}), which uniquely identify the constants of the window plane in the world reference frame; on the other side, the intrinsic parameters consist of the window thickness and the refractive index ratios at each side of the window itself. The latter were kept constant throughout the calibration procedure and equal to their nominal values: $t_w = 5$ mm, $\varrho_1 = 1/1.49$ and $\varrho_2 = 1.49/1.33$. It is worth remarking that, as shown by Belden [8], the calibration error function is fairly insensitive to changes in t_w for general camera network and significantly affected by changes in the refractive index ratio. In the present configuration, characterized by small angles of incidence of the LOSs on the planar windows (lower than $6°$) and correspondingly small refractive distortions, also a low sensitivity to the parameter z_{w_0} has been found. For this reason, in the pinhole+window calibration, such parameter was optimized separately from the others. By comparing the first and the second columns of Table 2, it is interesting to see that the reprojection errors for each camera remain nearly unaltered. This suggests that the only pinhole camera model would be sufficient to map the field-of-view with acceptable accuracy. Nevertheless, the introduction of the refractive windows in the perspective model allows the retrieval of the correct values of the focal lengths (≈ 30 mm versus ≈ 40 mm of the initial pinhole calibration).

Once calibrated the pinhole+window system, the cylinder parameters are estimated using data collected in step 2 of the calibration procedure. In particular, at this stage, both the 3D/2D coordinate pairs found in step 1, which are undistorted by the cylinder, and those found in step 2, which are distorted by the cylinder, are used to calibrate the extrinsic cylinder parameters and refine all the pinhole parameters. After the pinhole +window+cylinder calibration (third column of Table 2), the camera angles are only slightly modified, whereas the focus locations are affected by larger variations. Indeed, the latter are consistent with the slight variations (within $\pm 5°$) of the window angles with nearly unchanged camera angles. The greater root-mean-square reprojection errors (around 0.5 pixels or greater) are instead due to the greater errors related to the image detection of the cylinder-distorted markers (due to the image deformation of the dot shape).

In step 3 of the calibration procedure, all the model parameters, excluding the intrinsic window parameters and including the intrinsic cylinder parameters, are optimized. It is interesting to observe that the camera and cylinder parameters undergo only small adjustments, whereas more relevant variations are found for the window orientations. The residual reprojection errors after the volume self-calibration are less than 0.2 pixels and are essentially related to uncertainty in particle triangulation (apart from image noise).

As a final comment, it should be noticed that, in the present experimental setup, very similar results in terms of the estimated cylinder parameters and reprojection errors are obtained by neglecting the presence of the refractive windows (as done in previous works; e.g., [25]). Although it yields camera poses and optical focal lengths not to have a physical meaning (they correspond to the apparent point of view of an observer located in water and are near to the values reported in the first column of Table 2), the advantage is that the computational cost of the projection of 3D world points is reduced without a detrimental effect on the accuracy in tomographic reconstruction. For this reason, in the following tomographic PIV process, a refractive model based just on a pinhole+cylinder system has been used.

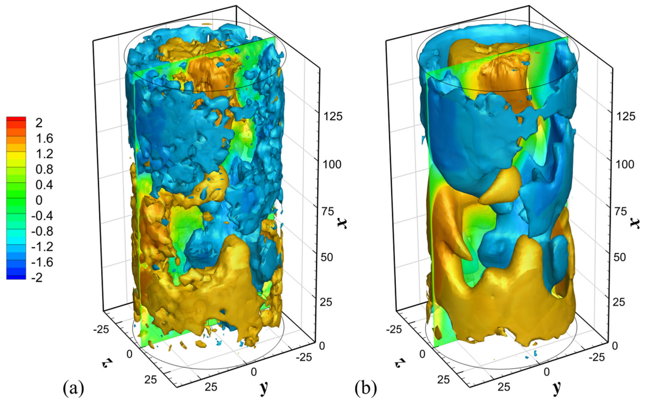

Fig. 7. Comparative tomographic reconstructions of the instantaneous velocity field obtained with (a) classical pinhole camera model and (b) refractive camera model. Isosurfaces of the x-velocity component. Velocity values are in mm/s, coordinates in mm.

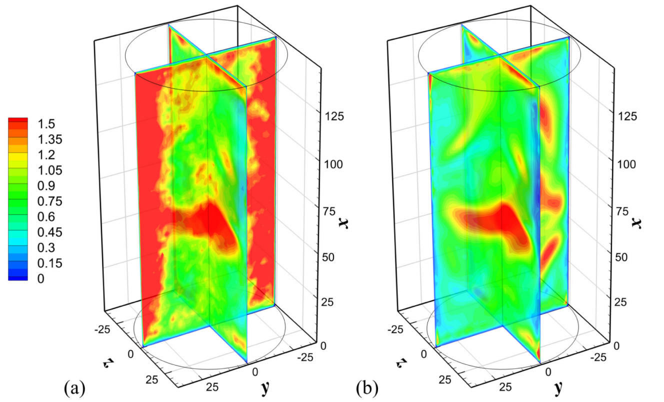

Fig. 8. Comparative tomographic reconstructions obtained with (a) classical pinhole camera model and (b) refractive camera model. Slices of the time-averaged field of the z-velocity component fluctuation at the xy and xz planes. Velocity values are in mm/s, coordinates in mm.

6.2 3D Tomographic Reconstruction

Fig. 7 shows an instantaneous snapshot of the evolution of the thermal convection inside the cylinder reconstructed with the classical pinhole camera model and the refractive camera model using similar process parameters. The convection is driven by a 5°C temperature difference between the bottom (heated by a copper slab coupled with a disc heater) and the top (cooled by a water heat exchanger), maintained constant with the aid of high-precision thermoelectric controller. The laser light is shaped into a cylindrical beam that illuminates the entire cell, passing through the transparent heat exchanger on the top; the fluid is seeded by polyethylene microspheres (Cospheric UVPMS-BO-1.00) with average particle diameter of 58 μm and particle density of 1.00 g/cc, resulting in a relaxation time lower than 1 ms. Time-resolved tomographic PIV measurements are carried out at a frequency of 7.5 Hz and processed with a method combining both algebraic tomographic reconstruction techniques (based on the sequential-motion-tracking enhancement algorithm from [26] with multi-resolution iterations of the SMART and CSMART algorithms [27] and multi-pass volumetric cross-correlation [28]) and advanced 4D particle tracking methods (Shake-The-Box method [29] and iterative particle identification [30]). The final structured velocity fields are determined by interpolating particle velocities along their trajectories, appropriately smoothed, using a second-order polynomial interpolation method.

In Fig. 7 the isosurfaces of the vertical velocity component (parallel to the cylinder axis) are represented. The velocity field reconstruction obtained with the classical pinhole camera model (Fig. 7a) appears to be extremely noisy over the entire domain compared to the camera model featuring the refraction correction (Fig. 7b). Indeed, fairly good results might be expected at least in the central portion of the cell since this region is imaged along LOSs which are affected by small refractive distortions. The highly distributed noise is explainable by considering that the parameters of the pinhole camera models used for the tomographic reconstruction were obtained initially from step 1 of the calibration procedure presented in the previous section (neglecting the presence of the windows) and then refined with the self-calibration procedure. Therefore, they are not representative of the real camera viewpoints, rather they correspond to viewpoints minimizing the disparity errors between the four cameras. However, it is interesting to see that the velocity field structure is not significantly altered or lost in the proximity of the cylinder sidewall, where the greater distortions occur.

Although not shown here for conciseness, when the velocity field is averaged over a sufficient number of snapshots, minor differences are found between the two examined camera models. This suggests that the noise in the instantaneous velocity field reconstruction of the pinhole camera model is smoothed out by the averaging process. However, this is not the case for second or higher order time statistics or time-derived quantities like fluid accelerations. In order to show this, Fig. 8 reports the reconstructions of the fields of the fluctuating z-velocity component averaged over a short time period (500 samples which correspond to little more than one minute in the present experiment). The figure shows that, while in the case of the refractive camera model the velocity fluctuations tends smoothly to zero approaching the cylinder sidewall, in the case of the pinhole camera model non-physical high fluctuations are observed in the regions near the sidewall in the xz plane.

7 Conclusion

This work has presented a calibration camera model for imaging through refractive geometries, which integrates the pinhole camera model with a refraction correction determined by applying Snell's law of refraction. The method shows greater robustness and faster convergence rate in the comparison with previous techniques available in the literature and is capable of handling the occurrence of total internal reflection along the optical path in the iterative solving procedure. A general approach for calibration of the camera model has been also outlined. The effects of image noise, volume size of the grid of calibration points and number of cameras on the non-linear least squares estimation of the refractive intrinsic and extrinsic parameters have been numerically analyzed in the case of a cylindrical configuration. Results show that when image noise is high and/or the volume size of the calibration grid is limited, a more robust approach consists in avoiding refinement of the intrinsic parameters and estimating only the extrinsic ones via image-based camera calibration; moreover, more accurate estimates are obtained by using a camera bundle.

An experimental verification of the present model has been made in relation to a tomographic PIV investigation of thermal convection inside a PMMA cylinder immersed in water. A specific calibration procedure for this setup, in which the cylinder interior is physically inaccessible, has been presented and thoroughly discussed. The validity of the method is proved by both the sensible values of the camera and body parameters and the accuracy in 3D velocimetry reconstruction in regions adjacent to the cylinder sidewall. A challenging aspect of the present application is that the calibrated camera model is used in a region (interior of the cylinder) where the refraction corrections have not been measured directly, thus, in some sense, the camera model is extrapolated to the measuring volume. Using such experimental data, the refractive camera model has also been compared to the classical pinhole camera model, which has been found to be inaccurate for obtaining reliable results although the moderate variation of the refractive index across the cylinder ($\varrho = 0.89$).

References

[1] S. Wiederseiner, N. Andreini, G. Epely-Chauvin, and C. Ancey, “Refractive-index and density matching in concentrated particle suspensions: A review,” *Experiments Fluids*, vol. 50, no. 5, pp. 1183–1206, 2011.

[2] N. Amini and Y. A. Hassan, “An investigation of matched index of refraction technique and its application in optical measurements of fluid flow,” *Experiments Fluids*, vol. 53, no. 6, pp. 2011–2020, 2012.

[3] Y. A. Hassan and E. Dominguez-Ontiveros, “Flow visualization in a pebble bed reactor experiment using PIV and refractive index matching techniques,” *Nuclear Eng. Des.*, vol. 238, no. 11, pp. 3080–3085, 2008.

[4] P. Miller, K. Danielson, G. Moody, A. Slifka, E. Drexler, and J. Hertzberg, “Matching index of refraction using a diethyl phthalate/ethanol solution for in vitro cardiovascular models,” *Experiments Fluids*, vol. 41, no. 3, pp. 375–381, 2006.

[5] A. Sedlazeck and R. Koch, “Perspective and non-perspective camera models in underwater imaging–overview and error analysis,” in *Proc. Outdoor Large-Scale Real-World Scene Anal.*, 2012, pp. 212–242.

[6] R. Kotowski, “Phototriangulation in multi-media photogrammetry,” *Int. Archives Photogrammetry Remote Sens.*, vol. 27, no. B5, pp. 324–334, 1988.

[7] C. Mulsow, “A flexible multi-media bundle approach,” *Int. Archives Photogrammetry Remote Sens. Spatial Inf. Sci.*, vol. 38, pp. 472–477, 2010.

[8] J. Belden, “Calibration of multi-camera systems with refractive interfaces,” *Experiments Fluids*, vol. 54, no. 2, 2013, Art. no. 1463.

[9] M. Feng, X. Jia, J. Wang, S. Feng, and T. Zheng, “Global calibration of multi-cameras based on refractive projection and ray tracing,” *Sensors*, vol. 17, no. 11, 2017, Art. no. 2494.

[10] H.-G. Maas and A. Gruen, “Digital photogrammetric techniques for high-resolution three-dimensional flow velocity measurements,” *Opt. Eng.*, vol. 34, no. 7, pp. 1970–1977, 1995.

[11] P. Westfeld and H.-G. Maas, “3-D least squares tracking in time-resolved tomographic reconstruction of dense flow marker fields,” in *Proc. Int. Archives Photogrammetry Remote Sens. Spatial Inf. Sci.*, 2010, vol. 1, pp. 597–602.

[12] R. Tsai, “A versatile camera calibration technique for high-accuracy 3D machine vision metrology using off-the-shelf TV cameras and lenses,” *IEEE J. Robot. Autom.*, vol. 3, no. 4, pp. 323–344, Aug. 1987.

[13] T. Melen, “Geometrical modelling and calibration of video cameras for underwater navigation,” Ph.D. dissertation, Dept. Eng. Cybern., Norwegian Univ. Sci. Technol., Trondheim, Norway, 1996.

[14] J. Heikkila and O. Silven, “A four-step camera calibration procedure with implicit image correction,” in *Proc. IEEE Comput. Soc. Conf. Comput. Vis. Pattern Recognit.*, 1997, pp. 1106–1112.

[15] R. Hartley and A. Zisserman, *Multiple View Geometry in Computer Vision*. Cambridge, U.K.: Cambridge Univ. Press, 2003.

[16] J. Weng, P. Cohen, and M. Herniou, “Camera calibration with distortion models and accuracy evaluation,” *IEEE Trans. Pattern Anal. Mach. Intell.*, vol. 14, no. 10, pp. 965–980, Oct. 1992.

[17] V. Usenko, N. Demmel, and D. Cremers, “The double sphere camera model,” in *Proc. Int. Conf. 3D Vis.*, 2018, pp. 552–560.

[18] J. J. Moré, “The Levenberg-Marquardt algorithm: Implementation and theory,” in *Proc. Numerical Anal.*, 1978, pp. 105–116.

[19] H.-G. Maas, “On the accuracy potential in underwater/multimedia photogrammetry,” *Sensors*, vol. 15, no. 8, pp. 18 140–18 152, 2015.

[20] T. Treibitz, Y. Schechner, C. Kunz, and H. Singh, “Flat refractive geometry,” *IEEE Trans. Pattern Anal. Mach. Intell.*, vol. 34, no. 1, pp. 51–65, Jan. 2012.

[21] A. Agrawal, S. Ramalingam, Y. Taguchi, and V. Chari, “A theory of multi-layer flat refractive geometry,” in *Proc. IEEE Conf. Comput. Vis. Pattern Recognit.*, 2012, pp. 3346–3353.

[22] G. Paolillo, “Experimental and numerical investigation of Rayleigh-Bénard convection,” Ph.D. dissertation, Dept. Ind. Eng., Università degli Studi di Napoli “Federico II”, Naples, Italy, 2018.

[23] B. Wieneke, “Volume self-calibration for 3D particle image velocimetry,” *Experiments Fluids*, vol. 45, no. 4, pp. 549–556, 2008.

[24] S. Discetti and T. Astarita, “The detrimental effect of increasing the number of cameras on self-calibration for tomographic PIV,” *Meas. Sci. Technol.*, vol. 25, no. 8, 2014, Art. no. 084001.

[25] E. S. Harvey and M. R. Shortis, “Calibration stability of an underwater stereo-video system: Implications for measurement accuracy and precision,” *Marine Technol. Soc. J.*, vol. 32, no. 2, pp. 3–17, 1998.

[26] K. P. Lynch and F. Scarano, “An efficient and accurate approach to MTE-MART for time-resolved tomographic PIV,” *Experiments Fluids*, vol. 56, no. 3, 2015, Art. no. 66.

[27] G. Castrillo, G. Cafiero, S. Discetti, and T. Astarita, “Blob-enhanced reconstruction technique,” *Meas. Sci. Technol.*, vol. 27, no. 9, 2016, Art. no. 094011.

[28] S. Discetti and T. Astarita, “A fast multi-resolution approach to tomographic PIV,” *Experiments Fluids*, vol. 52, no. 3, pp. 765–777, 2012.

[29] D. Schanz, S. Gesemann, and A. Schröder, “Shake-The-Box: Lagrangian particle tracking at high particle image densities,” *Experiments Fluids*, vol. 57, no. 5, 2016, Art. no. 70.

[30] B. Wieneke, “Iterative reconstruction of volumetric particle distribution,” *Meas. Sci. Technol.*, vol. 24, no. 2, 2012, Art. no. 024008.

Gerardo Paolillo received the master’s degree in aerospace engineering and the PhD degree in industrial engineering from the Università di Napoli “Federico II,” Italy, in 2015 and 2018, respectively, where he is currently a postdoctoral fellow at the Department of Industrial Engineering. His research interests include the area of experimental fluid mechanics, with focus on applications of unsteady jets to flow control and electronics cooling, investigation into dynamics of turbulent Rayleigh-Bènard convection and development of 3D optical velocimetry techniques.

Tommaso Astarita received the master’s degree in aeronautical engineering and the PhD degree in aerospace engineering from the Università di Napoli “Federico II,” Italy, in 1993 and 1997, respectively. He was a postdoctoral fellow with the von Kármán Institute for Fluid Dynamics, Belgium and is currently a full professor of fluid mechanics at the Università di Napoli “Federico II.” His main research interests include the experimental study of problems in the fields of fluid mechanics and convective heat transfer, in particular, the application and development of IR thermography and stereoscopic and tomographic PIV techniques for fluid mechanics problems.

Open Access funding provided by Universita degli Studi di Napoli “Federico II” within the CRUI CARE Agreement